Upraising the O 2p Orbital by Integrating Ni with MoO₂ for Accelerating Hydrogen Evolution Kinetics

Xiong Liu,[†,∥] Kun Ni,[‡,∥] Chaojiang Niu,[†,∥] Ruiting Guo,[†] Wei Xi,[*,§] Zhaoyang Wang,[†] Jiashen Meng,[†] Jiantao Li,[†] Yanwu Zhu,[‡] Peijie Wu,[†] Qi Li,[†] Jun Luo,[§] Xiaojun Wu,[*,‡] and Liqiang Mai[*,†]

[†]State Key Laboratory of Advanced Technology for Materials Synthesis and Processing, Wuhan University of Technology, Wuhan 430070, People's Republic of China

[‡]Hefei National Laboratory for Physical Sciences at the Microscale, School of Chemistry and Materials Sciences, CAS Key Laboratory of Materials for Energy Conversion, CAS Center for Excellence in Nanoscience, iChEM (Collaborative Innovation Center of Chemistry for Energy Materials), University of Science and Technology of China, Hefei, Anhui 230026, People's Republic of China

[§]Center for Electron Microscopy and Tianjin Key Laboratory of Advanced Functional Porous Materials, Institute for New Energy Materials & Low-Carbon Technologies, School of Materials Science and Engineering, Tianjin University of Technology, Tianjin 300384, People's Republic of China

S *Supporting Information*

ABSTRACT: Unique interfacial properties within heterostructures play vital roles in enhancing hydrogen evolution reaction (HER) electrocatalysis. On the basis of the MoO₂-Ni heterostructure, we hereby propose an upraised atomic orbital promoted catalytic mechanism for accelerating the HER kinetics. A controllable gradient-pyrolysis approach is adopted on molybdates to integrate Ni with MoO₂, possessing numerous phase-separation-induced intimate interfaces. In situ characterizations demonstrate the formation process of MoO₂-Ni interfaces and excellent compositional stability under alkaline conditions. The optimized MoO₂-Ni catalyst delivers remarkable Pt-like HER activity and good stability with 50 h operation in 1 M KOH. An enhancement of 3 orders of magnitude on the exchange current density is achieved for MoO₂-Ni in comparison to the simplex MoO₂. Further experimental and theoretical analyses verify the existence of a concentrated surface charge at MoO₂-Ni interfaces. Meanwhile, with the incorporation of Ni into MoO₂, the most active sites dramatically change from Mo to O atoms at MoO₂-Ni interfaces. The Ni contact upraises the O 2p orbital in MoO₂, thus strengthening the hydrogen adsorption for enhanced HER kinetics.

KEYWORDS: *heterostructure, upraised orbital, enhanced hydrogen adsorption, hydrogen evolution reaction, catalytic mechanism*
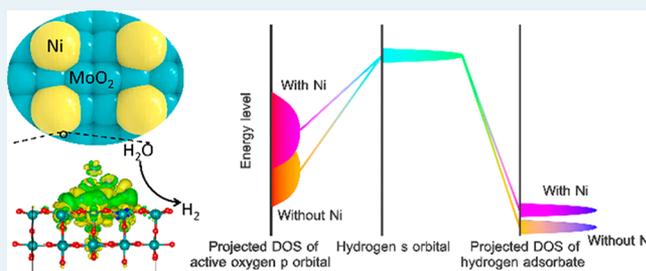
INTRODUCTION

Hydrogen is generally regarded as a promising alternative to fossil fuels; the electrocatalytic hydrogen evolution reaction (HER) is in the forefront of research as the most sustainable method to produce H₂.[1−3] Currently, the "Holy Grail" HER electrocatalysts are still Pt-based materials, but their natural scarcity and unsatisfactory catalytic durability greatly hamper their large-scale commercialization.[4,5] Though great advances in non-precious-metal-based electrocatalysts have been achieved recently, the exploration of highly efficient and earth-abundant HER electrocatalysts remains in high demand.[6−8] The Sabatier principle, which gives a qualitative description of an optimal catalyst, shows that a catalyst with a high HER activity should possess moderate bonding to the reactive intermediate.[9,10] Accordingly, recent research in this field has headed in this direction. As the catalytic kinetics is dependent on the surface state of a catalyst, generally it can be greatly enhanced via a synergistic effect by interfacing different

components.[11] At the same time, integrating one component with another to form a heterostruture will result in an interfacial charge polarization due to the different work functions, which modulates the surface charge states of catalysts and then the bonding with reactive intermediates.[11,12] The heterostructure endowed with anisotropic transport properties is highly beneficial for diverse applications in batteries,[13] capacitors,[14] catalysis,[15] and so on. Heterostructured catalysts, such as metal (oxide)−metal (oxide),[16−19] metal (oxide)−compound,[20−24] and compound−compound,[25−28] commonly display superior catalytic performance in comparison to their simplex counterparts. Consequently, the design and construction of chemically disparate materials have received extensive attention for optimizing catalytic perform-
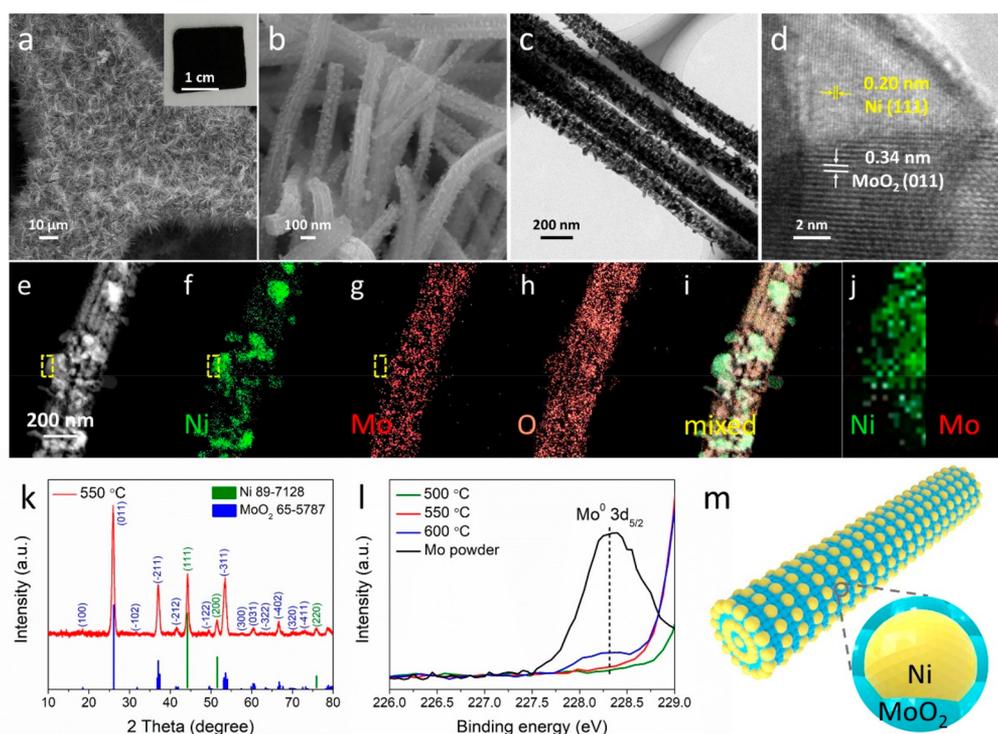
Figure 1. (a, b) SEM images of MoO$_2$-Ni-550 NWs/NF. The inset in (a) is the optical photo of MoO$_2$-Ni-550 NWs/NF. (c) TEM, (d) HRTEM, and (e−i) HAADF-STEM images with elemental mappings of MoO$_2$-Ni-550 nanowires. (j) Enlarged elemental mappings originating from the yellow dotted box areas in (e)−(g). (k) XRD pattern of MoO$_2$-Ni-550 powders. (l) Mo 3d XPS spectra of MoO$_2$-Ni-x (x = 500, 550 and 600) NWs and Mo powders. (m) Schematic illustration of a MoO$_2$-Ni heterogeneous nanowire.

ances. For example, Markovic and co-workers achieved enhanced electrocatalytic HER activity by tailoring Li$^+$-Ni(OH)$_2$-Pt interfaces.[24] Zhu and co-workers recently reported a Co-Ni$_3$N heterostructure with epitaxial interface interactions for improved HER performance.[20] Nevertheless, the underlying catalytic mechanism including the optimized hydrogen adsorption for catalyzing HER using heterostructures still requires in-depth investigation.

Metal oxide−metal heterostructured materials are known to play an important role in electrocatalysis,[29] water-gas shift reactions,[30] and organic electronic devices[31] as a result of their strong metal oxide−metal interactions, yet relatively few works have focused on their HER application. Some progress has been achieved on metal oxide−metal electrocatalysts such as Co-Co$_3$O$_4$,[32] Ni-CeO$_2$[33] and NiO-Ni,[19,34] realizing a superior catalytic activity in comparison to the single-component metal oxide or metal catalyst toward the HER. For example, the NiO/Ni interfaces in the NiO/Ni-CNT catalyst are proposed to be synergistically active sites for HER catalysis.[19] Although significant progress has been made, the catalytic sites and synergistic effects in these heterostructures still call for in-depth research to guide the further rational design of catalysts. Previous reports indicate that the Gibbs free energy of hydrogen adsorption (ΔG_{H*}) value for Ni is negative (−0.27 eV[35] or −0.55 eV[36]), while that for MoO$_2$ is positive (0.15 eV[37]). Therefore, it is expected that the generated interfaces in a MoO$_2$-Ni heterostructure would become efficient catalytic sites for fast hydrogen adsorption/desorption. Actually, a synergistic interaction between nickel clusters and molybdenum oxide support can lead to high water-gas shift reaction activity.[30] The component stability and enhanced HER

mechanism of the MoO$_2$-Ni heterostructure for alkaline HER also need further investigation.

Herein, we constructed a MoO$_2$-Ni heterostructure and uncovered its metal oxide−metal interactions as well as catalytic mechanism toward the HER. MoO$_2$-Ni nanowire arrays on nickel foam (denoted as MoO$_2$-Ni NWs/NF) were fabricated via a controlled gradient pyrolysis of molybdates. During in situ pyrolysis processes, numerous MoO$_2$-Ni intimate interfaces could be formed, where MoO$_2$ strongly interacts with the adjacent Ni. As a result, the MoO$_2$-Ni NWs/NF exhibits a Pt-like HER activity with superior catalytic stability of over 50 h in alkaline solution. Importantly, a 3 orders of magnitude enhancement on exchange current density is achieved for MoO$_2$-Ni in comparison to MoO$_2$. Furthermore, mechanistic insights into the catalytic sites and activity enhancement were first explored via experimental and theoretical analyses.

■ RESULTS

Synthesis and Characterizations of MoO$_2$-Ni Nanowire Arrays. A two-step procedure, namely fabrication of NiMoO$_4$·xH$_2$O nanowire arrays and subsequent phase-separation reactions via controlled gradient pyrolysis, was utilized to construct the MoO$_2$-Ni nanowire arrays. Before calcination, a monocrystalline NiMoO$_4$·xH$_2$O nanowire precursor with a smooth surface is uniformly grown on nickel foam (Figure S1 in the Supporting Information). After the pyrolysis treatment at 550 °C in Ar/H$_2$ (95/5 vol %) atmosphere (denoted as MoO$_2$-Ni-550), the morphology-preserved MoO$_2$-Ni nanowires fully cover the entire nickel foam (Figure 1a) and the bulged Ni nanoparticles clearly appear on the nanowires (Figure 1b,c). The perfect
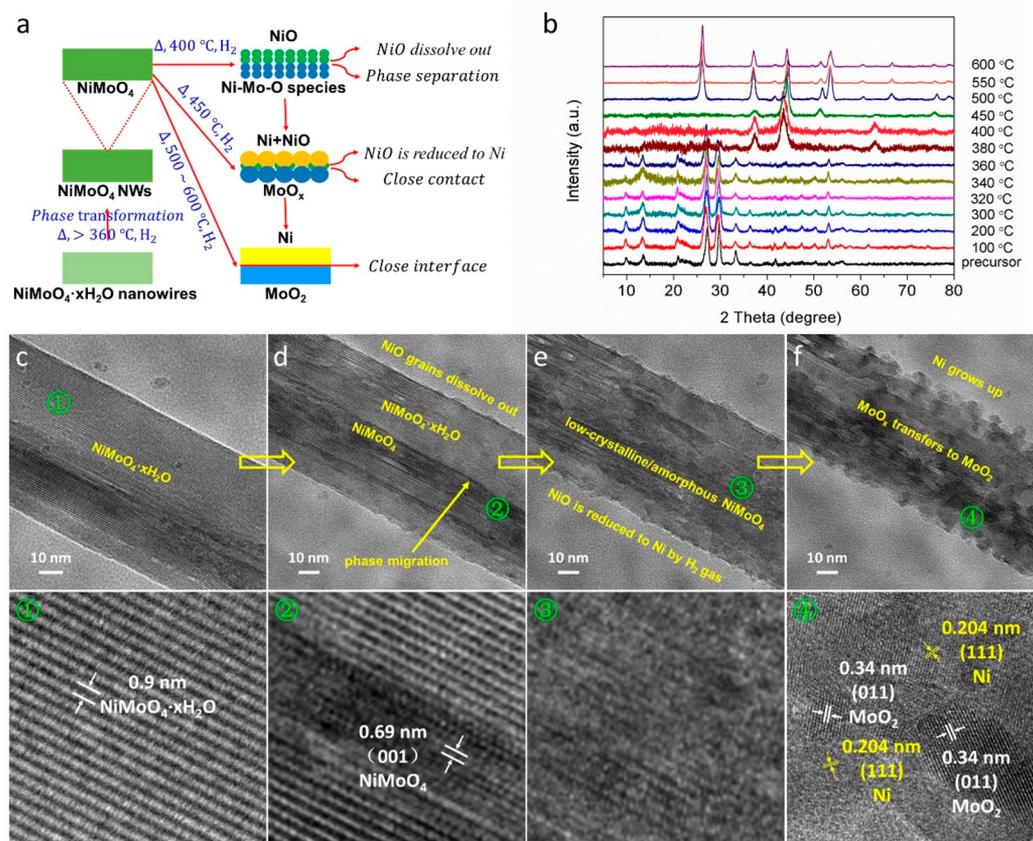
Figure 2. (a) Schematic illustration of the formation processes for MoO$_2$-Ni heterostructure. (b) Ex situ XRD patterns of the NiMoO$_4$·xH$_2$O precursor calcined at different temperatures. Representative in situ high-temperature TEM images of the precursor calcined at (c) 380 °C, (d) 400 °C, (e) 450 °C, and (f) 550 °C in Ar/H$_2$, respectively.

maintenance of nanowires is attributed to the microscopic heterogeneous components, which restrict the phase migration and particle aggregation.[13] The fine structure of MoO$_2$-Ni-550 nanowires is verified by electron microscope images (Figure 1d−j). A high-resolution transmission electron microscopy (HRTEM) image shows the intimate contact between MoO$_2$ and Ni. The lattice fringes of 0.34 and 0.20 nm are well-indexed to the (011) plane of MoO$_2$ (JCPDS No. 65-5787) and the (111) plane of Ni (JCPDS No. 89-7128), respectively. The phase-separated characteristics in the MoO$_2$-Ni nanowires are also established by a high-angle annular dark-field scanning transmission electron microscopy (HAADF-STEM) image with the corresponding energy-dispersive X-ray (EDX) mappings. The MoO$_2$ is mainly distributed in the nanowire backbone with the protuberant Ni nanoparticles closely attached. The enlarged mappings in Figure 1j originating from the yellow dotted box area suggest the absence of Mo-Ni alloys. The crystal structure and chemical states of the MoO$_2$-Ni catalyst were analyzed by X-ray diffraction (XRD) and X-ray photoelectron spectroscopy (XPS). Figure 1k presents the MoO$_2$ and Ni phases in the XRD pattern for the MoO$_2$-Ni nanowires. To further determine the likely existence of Mo-Ni alloys, the Mo 3d XPS spectra for the MoO$_2$-Ni nanowires obtained at different calcination temperatures were analyzed (Figure 1l). It can be found that the Mo-Ni alloys form only when the pyrolysis temperature reaches 600 °C during synthesis. At this calcination temperature, the MoO$_2$ is further reduced to low-valence molybdenum oxides or Mo^0; thus the

thermally stable Mo-Ni alloys start to form at this stage. For example, an obvious MoNi phase (JCPDS No. 65-6903) is observed on calcination at 800 °C (Figure S2 in the Supporting Information). Consequently, a MoO$_2$-Ni heterostructure with an immiscible phase separation can be obtained at a relatively low temperature (<600 °C). The Ni/Mo molar ratios of MoO$_2$-Ni-x (x = 500, 550, 600) are close to 1 according to the inductively coupled plasma (ICP) measurements (Figure S3 in the Supporting Information). Considering that the metallic Ni is unstable in acid, the acid-etching treatment was applied to uncover the distribution of MoO$_2$ in the MoO$_2$-Ni nanowires (Figure S4 in the Supporting Information). After treatment in 0.5 M H$_2$SO$_4$ for 2 days, mesoporous MoO$_2$ nanowire arrays consisting of ~30 nm nanoparticles are obtained. Therefore, we conclude that the MoO$_2$ nanoparticles form the backbone of the nanowire, with the Ni nanoparticles embedded in the MoO$_2$ nanowire as illustrated in Figure 1m.

Evolution Mechanism of MoO$_2$-Ni Heterostructured Nanowires. Here, the calcination-temperature-dependent morphology evolution of MoO$_2$-Ni heterostructure was investigated. The formation procedure of MoO$_2$-Ni nanowires is schematically illustrated in Figure 2a and was verified by ex situ XRD (Figure 2b and Figure S5 in the Supporting Information) and in situ high-temperature TEM (Figure 2c−f). The microstructure and phase evolutions of the nickel molybdate precursor (NiMoO$_4$·xH$_2$O) during the transformation to an MoO$_2$-Ni heterostructure are mainly divided
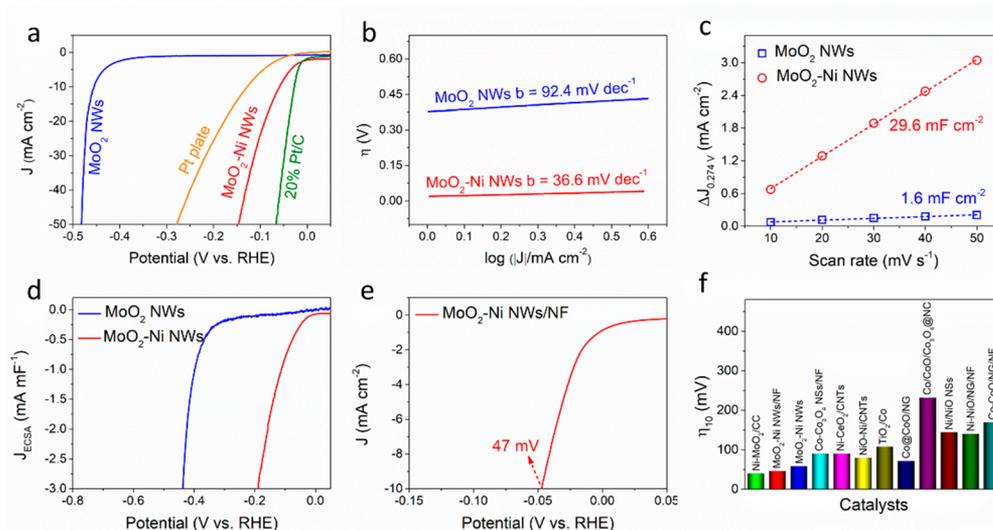
Figure 3. (a) LSV curves of MoO_2 NWs, MoO_2-Ni-550 NWs, Pt plate (size 1 cm × 1 cm), and 20 wt % Pt/C at 2 mV s^{-1} in 1 M KOH. (b) Tafel plots of MoO_2 NWs and MoO_2-Ni-550 NWs. (c) Charging current density differences ($\Delta j = j_a - j_c$) as a function of the scan rate. (d) LSV curves normalized by ECSA. (e) LSV curve of MoO_2-Ni-550 NWs/NF. (f) Overpotentials of MoO_2-Ni-550 NWs and MoO_2-Ni-550 NWs/NF at −10 mA cm^{-2} in 1 M KOH in comparison with some recently reported metal oxide−metal HER electrocatalysts.

into three stages. (1) The phase transformation of $NiMoO_4 \cdot xH_2O$ into $NiMoO_4$ happens until 380 °C, immediately followed by the outward dissolution of the NiO grains (400 °C). (2) The $NiMoO_4$ region becomes low crystalline/amorphous while the NiO is gradually reduced to Ni. (3) The MoO_x is reduced to MoO_2, the Ni nanoparticles grow, and finally the mesoporous MoO_2-Ni heterostructured nanowires are obtained. The detailed evolutions and in situ TEM snapshots of intermediates during the calcination processes are also clearly shown in Figures S6−S9 in the Supporting Information. In addition, $NiMoO_4$ is obtained as the final product after calcining the precursor under an Ar atmosphere (Figure S10 in the Supporting Information), which indicates the important role of the reducing atmosphere in the phase separation. This in situ pyrolysis and phase separation of polymetallic oxides (such as molybdate,[16,38,39] vanadate,[40] silicate,[41] and cerate[33]) promote the formation of numerous intimate interfaces, and thus, these oxides can be utilized to fabricate heterostructured materials. For instance, MoO_2-Ag heterogeneous nanowires can also be fabricated by a molybdate pyrolysis method (Figure S11 in the Supporting Information).

Synergistic Enhancement of HER Kinetics. The electrocatalytic activity of the MoO_2-Ni NWs catalyst toward the HER was analyzed in 1 M KOH using a standard three-electrode system. The MoO_2 catalyst and commercial Pt/C (20 wt % Pt on Vulcan XC-72R) with the same mass loadings as well as Pt plate were also studied for comparison. All of the polarization curves were corrected for iR compensation to remove the influence of ohmic resistance.[42,43] At an optimized mass loading of ∼1.5 mg cm^{-2} (Figure 3a and Figure S12 in the Supporting Information), the MoO_2-Ni NWs catalyst exhibits a remarkably low overpotential of 58.4 mV to deliver a current density of −10 mA cm^{-2} (η_{10} = 58.4 mV), which is much smaller than that for the MoO_2 NWs (454.3 mV). The reported metallic Ni as an alkaline HER catalyst generally needs an η_{10} value of larger than 150 mV with a large Tafel slope.[19,44,45] Therefore, the excellent catalytic performance of MoO_2-Ni is mainly attributed to the synergistic effect between

MoO_2 and Ni. The catalytic kinetics and inherent HER activities of catalysts have also been analyzed. The Tafel slope of MoO_2 in Figure 3b is substantially higher (92.4 mV dec^{-1}), suggesting a sluggish Volmer step (M + H_2O + e$^-$ → M − H + OH$^-$, where M represents the catalyst). However, it decreases to 36.6 mV dec^{-1} for MoO_2-Ni, indicating the Volmer−Tafel mechanism as the HER pathway.[46] With a low Tafel slope, the HER kinetics of the MoO_2-Ni catalyst is rapidly enhanced with increasing applied potential, which is advantageous for practical applications.[47] Remarkably, the exchange current density (j_0) of 0.307 mA cm^{-2} derived from the Tafel slope[46] for MoO_2-Ni is significantly larger than that of MoO_2 (8.15 × 10^{-5} mA cm^{-2}), demonstrating its superior intrinsic electrocatalytic activity.

The electrochemical double-layer capacitance (C_{dl}) is a key parameter to reflect the electrochemically active surface area (ECSA) of catalysts, which was estimated by collecting cyclic voltammetry (CV) curves in a non-Faradaic region of 0.224−0.324 V vs reversible hydrogen electrode (RHE) (Figure 3c and Figure S13 in the Supporting Information). The C_{dl} value for MoO_2-Ni-550 NWs (29.6 mF cm^{-2}) is much larger than that for MoO_2 NWs (1.6 mF cm^{-2}), indicating that the former allows more effective accessibility to active sites. To evaluate the real activity of catalysts, the LSV curves were normalized by ECSA. As shown in Figure 3d, the MoO_2-Ni-550 NWs catalyst exhibits higher HER activity. In addition, the catalyst grown in situ on the substrate can expose more sites and promote catalysis,[7,48,49] meanwhile, the three-dimensional array architecture also contributes to the enhanced mass diffusion. As a result, the as-prepared MoO_2-Ni-550 NWs/NF catalyst can achieve optimal HER performance with η_{10} = 47 mV (Figure 3e), which is comparable with that of the commercial Pt/C (η_{10} = 27 mV) and superior to that of the Pt plate (η_{10} = 128 mV). In comparison with reported non-precious-metal oxide−metal catalysts, the MoO_2-Ni catalyst exhibits the best HER activity, which suggests the importance of the unique interaction between MoO_2 and Ni (Figure 3f and Table S1 in the Supporting Information).
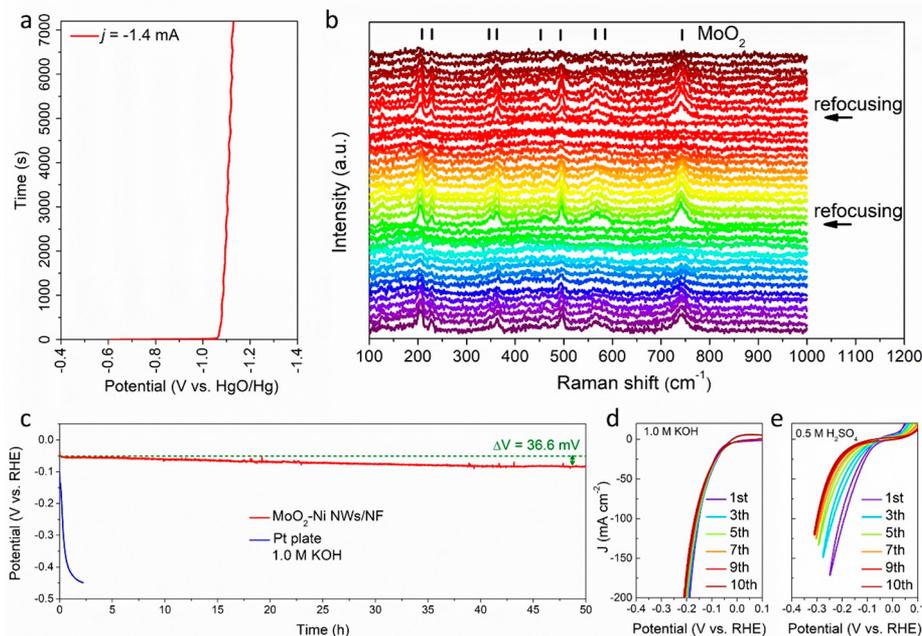
Figure 4. (a) Chronopotentiometric measurement of MoO$_2$-Ni-550 NWs/NF at −1.4 mA in 1 M KOH during in situ Raman testing. (b) Corresponding in situ Raman spectra. (c) Chronopotentiometric measurement of MoO$_2$-Ni-550 NWs/NF and Pt plate at −10 mA cm^{-2} in 1 M KOH. (d, e) CV curves of MoO$_2$-Ni-550 NWs/NF tested at a scan rate of 5 mV s^{-1} in 1 M KOH and 0.5 M H$_2$SO$_4$, respectively.

We have also investigated the effect of pyrolysis temperature of the MoO$_2$-Ni catalysts toward HER activity. The MoO$_2$-Ni prepared at the moderate pyrolysis temperature of 550 °C achieves the optimal HER activity (Figure S14 in the Supporting Information), which is attributed to its high electronic conductivity, mesoporous structure, and abundant active interfaces. The microstructures and electron conductivity of the final products at different pyrolysis temperatures (550, 550, and 600 °C) have been further analyzed (Figures S15−S17 in the Supporting Information). A lower calcination temperature of 500 °C results in a well-retained nanowire structure with low electronic conductivity of catalysts, while a higher calcination temperature of 600 °C leads to excessive interconnection with partial miscibility existing as Mo-Ni alloys. The destroyed heterostructure and closed pore structure reduces the number of nanoscale MoO$_2$-Ni interfaces. Though the Brunauer−Emmett−Teller (BET) of value MoO$_2$-Ni-500 (70.1 m^2 g^{-1}) is slightly larger than that of MoO$_2$-Ni-550 (54.4 m^2 g^{-1}), the latter possesses 1 order of magnitude higher electronic conductivity, which increases the electron transfer rate during the catalytic processes. From the XPS analyses (Figure S18 in the Supporting Information), the higher electronic conductivity of MoO$_2$-Ni-550 can be attributed to the relatively high metallic Ni content. Moreover, MoO$_2$-Ni-600 possesses the smallest exposed surface area of 17 m^2 g^{-1}. Its severe aggregation leads to a greatly reduced pore volume as low as 0.03 m^3 g^{-1}, which causes a large number of active interfaces to be covered. Therefore, the HER activities of these electrocatalysts exhibit the following trend: MoO$_2$-Ni-550 > MoO$_2$-Ni-500 > MoO$_2$-Ni-600. As discussed above, a balance between the electronic conductivity and heterogeneous microstructure is vital for realizing the optimal catalytic performance.

Roles of the MoO$_2$-Ni Interfaces in HER Activities. A coupled Raman−electrochemistry system was assembled to track the evolution of catalysts in real time. To verify the component stability of the MoO$_2$-Ni-550 catalyst, the chronopotentiometric measurements were conducted at a constant current of −1.4 mA during the in situ Raman test. The potential exhibits a slight variation in the 7000 s testing, which indicates good operating conditions (Figure 4a). According to Figure 4b, the initial well-defined Raman peaks at 207, 230, 348, 365, 497, 568, 585, and 740 cm^{-1} belong to the monoclinic MoO$_2$,[37,50,51] indicating the pure phase of the MoO$_2$-Ni catalyst. However, these peaks gradually disappear after a continuous testing of ∼2000 s. This phenomenon is attributed to the generated H$_2$/O$_2$ bubbles in the solution during the electrocatalytic measurement, and these bubbles can change the pathway of the Raman laser and thus result in focusing error. The strong Raman peaks for MoO$_2$ are observed again after refocusing without changing the horizontal position of the MoO$_2$-Ni sample. Also, the absence of Raman peaks for other molybdenum oxides (such as MoO$_3$ and Mo$_4$O$_{11}$) and nickel oxides/hydroxides demonstrates the stability of the MoO$_2$-Ni catalyst during HER testing in 1 M KOH. The stability of MoO$_2$-Ni-550 NWs/NF was also evaluated by chronopotentiometry at −10 mA cm^{-2} in 1 M KOH in a standard three-electrode system (Figure 4c). The MoO$_2$-Ni catalyst exhibits considerable catalytic stability with a small increase of 36.6 mV in η_{10} after 50 h of continuous testing. In comparison, the rapidly increased overpotential for the Pt plate is observed during the 8000 s, indicating the catalytic instability of the Pt catalyst, which is consistent with previous reports.[7,47] The stability of MoO$_2$-Ni-550 NWs/NF is also reflected by CV in alkaline solutions (Figure 4d). The negligible change in the CV curves at different cycles in 1 M KOH demonstrates the well-maintained HER activity. In addition, the LSV curves after soaking in 1 M KOH for different durations also display small changes, further indicating the stable catalytic performance of MoO$_2$-Ni catalyst (Figure S19a in the Supporting Information). However, the HER activity of MoO$_2$-Ni-550 NWs/NF rapidly decreases
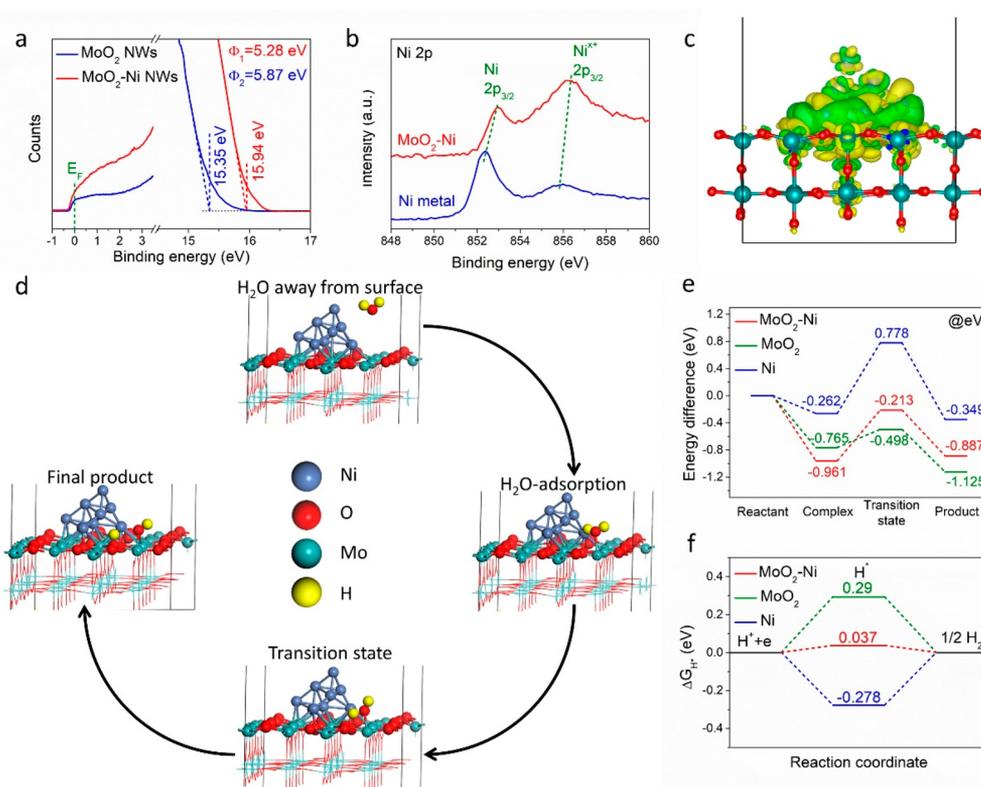
Figure 5. (a) UPS spectra of MoO_2-Ni and MoO_2 nanowires. (b) Ni 2p XPS spectra of MoO_2-Ni and Ni. (c) Differential charge density of MoO_2-Ni. The green contour represents the charge accumulation. (d) Optimized structure models for MoO_2-Ni with four water-dissociation steps. The blue, green, red, and yellow balls refer to Ni, Mo, O, and H atoms, respectively. (e) Corresponding energy differences of MoO_2-Ni, MoO_2, and Ni models during four water-dissociation steps. (f) ΔG_{H*} calculated at the equilibrium potential of MoO_2-Ni, MoO_2, and Ni models.

when it is measured in acid with cycling (Figure 4e and Figure S19b in the Supporting Information). As determined by the ICP measurements, the Ni/Mo ratio decreases rapidly until all the Ni contents are dissolved (Figure S20 in the Supporting Information). Since MoO_2 is stable in 0.5 M H_2SO_4, the above result indicates the dissolution of Ni and hence decreases the MoO_2-Ni interfaces. In addition, the effective active surface area of MoO_2-Ni-550 NWs/NF was evaluated by CV measurements (Figure S21 in the Supporting Information). The initial C_{dl} value of the MoO_2-Ni NWs/NF measured in 1 M KOH is 102.2 mF cm^{-2}. However, the C_{dl} values decrease to 86.0, 54.7, and 19.7 mF cm^{-2} after soaking in 0.5 M H_2SO_4 for 12, 18, and 24 h, respectively. Therefore, the decreased effective active area of MoO_2-Ni NWs/NF is a result of the dissolution of Ni in acid, thus leading to the reduction of active MoO_2-Ni interfaces and decay of HER activity.

To further reveal the structure−performance correlation, ultraviolet photoelectron spectroscopy (UPS) measurements were employed to study the valence band electrons of the MoO_2-Ni catalyst, as depicted in Figure 5a. The MoO_2-Ni has a smaller work function (Φ) of 5.28 eV in comparison with that of MoO_2 (5.87 eV), indicating the electron transfer from Ni to MoO_2 and thus increasing the Fermi level energy. The lower work function and the increased Fermi level energy can strengthen the chemical adsorption of hydrogen and thus promote the HER processes. Generally, the binding energy of the materials correlates negatively with the surface electron density; hence, the electron transfer can also be reflected by XPS measurements.[20,52] Before the comparison, the C 1s XPS peaks of all samples were first calibrated to be 284.5 eV. The Ni 2p peaks in the MoO_2-Ni heterostructure show a positive

shift (∼0.5 eV) in comparison with that of Ni, indicating the electron donation from Ni to MoO_2 (Figure 5b). Meanwhile, the Mo 3d peaks shift positively (∼0.2 eV, Figure S22 in the Supporting Information) after removing Ni from MoO_2-Ni via an acid treatment.

Theoretical Investigation of the Roles of Interfaces toward HER. To identify the synergistic effect in heterostructured catalysts, computational simulations are beneficial in uncovering adsorption/desorption energy of reactive intermediates, catalytic sites and so on.[53−56] We carried out density functional theory (DFT) calculations on MoO_2 (011)-Ni, MoO_2 (011), and Ni (111) models according to the experimental results (Figure S23 in the Supporting Information). First, the integrated charge density difference yields a charge concentration enhanced area at the MoO_2-Ni interface, indicating a tailored electronic structure which differs from the simplex MoO_2 and Ni (Figure 5c). This phenomenon is induced by the charge polarization on integrating Ni and MoO_2. The free energy diagram showcases the four water dissociation steps at the MoO_2-Ni interface: namely, H_2O away from the surface, H_2O adsorption, transition state, and final product (Figure 5d,e and Figure S24 in the Supporting Information). The low water dissociation kinetic energy barrier (ΔG_w) of 0.748 eV for MoO_2-Ni indicates fast water dissociation steps. This value is lower than that for Ni (1.04 eV) and those previously reported for other high-efficiency HER catalysts.[57−59] Generally, a high-efficiency HER catalyst should also possess moderate hydrogen adsorption with a ΔG_{H*} of near zero.[9,60,61] Only the ΔG_{H*} values calculated at the MoO_2-Ni interface are close to zero from a screening of the possible catalytic sites, which include the sites on the MoO_2
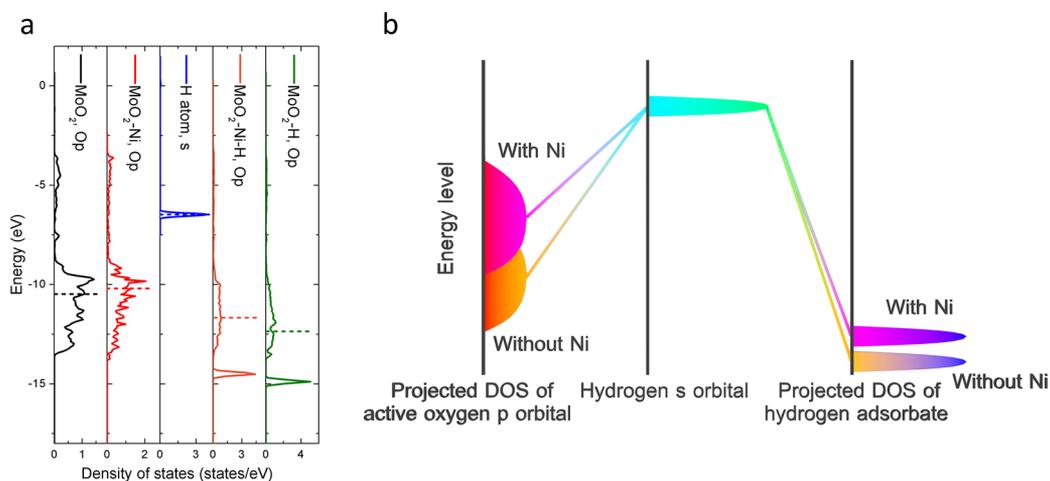
Figure 6. Upraised atomic orbital-promoted catalytic mechanism. (a) PDOS (taking the vacuum energy level as zero) for the oxygen's p orbital of the MoO_2 model (MoO_2, Op), oxygen's p orbital of the MoO_2-Ni model (MoO_2-Ni, Op), hydrogen's s orbital (H atom, s), oxygen's p orbital of the H-adsorbed MoO_2 model (MoO_2-H, Op), and oxygen's p orbital of the H-adsorbed MoO_2-Ni model (MoO_2-Ni-H, Op). The dotted lines represent the p-band center of the O atom and s-band center of the H atom. (b) Schematic diagram showing the bonding interaction of active sites and hydrogen atom based on the PDOS results in (a). The energy levels of all orbitals take the vacuum energy level as zero.

and Ni and away from the interface (Figure 5f and Figure S25a in the Supporting Information). In addition, the strongly positive and negative ΔG_{H*} values of the respective MoO_2 and Ni suggest sluggish HER kinetics associated with the poor HER activity in the experiments. Therefore, the tailored MoO_2-Ni interfaces are determined to be the effective HER catalytic sites.

In addition, the most active site dramatically shifts from the Mo atom in the MoO_2 model to the O atom at the interface in the MoO_2-Ni model. To explore the active origin of surface oxygen, the projected density of states (PDOS) of MoO_2-Ni and MoO_2 surface was analyzed (Figure 6a). In comparison with that in pure MoO_2, the oxygen's p orbital is upraised and comes nearer to hydrogen's s orbital in the MoO_2-Ni model. After hydrogen adsorption, the oxygen's p orbital in the MoO_2-Ni-H model is also upraised. This indicates that the hydrogen−oxygen interaction becomes stronger after Ni incorporation. Considering that the hydrogen adsorption on the MoO_2 surface is too weak to boost the HER, the introduction of Ni can therefore accelerate the HER kinetics. According to the PDOS results, a schematic illustration of the origin for enhanced HER activity from the electronic structure aspect is shown in Figure 6b. It shows that the Ni contact leads to the upraised O 2p orbital of MoO_2 and thus stronger hydrogen adsorption for accelerating HER kinetics.

Evaluation of Water-Splitting Performance Based on MoO_2-Ni-550 NWs/NF (Cathode) and NiFe-S/CC (Anode). The obtained MoO_2-Ni-550 NWs/NF and the synthesized nickel−iron sulfide nanosheets grown on carbon cloth (NiFe-S/CC) were used as the cathode and anode to evaluate the water splitting application in alkaline solution. The obtained NiFe-S/CC is characterized in detail as shown in Figure S27 in the Supporting Information. In 1 M KOH, NiFe-S/CC exhibits excellent oxygen evolution reaction (OER) catalytic stability with a low overpotential of about 1.48 V at 10 mA cm^{-2} and well-maintained nanosheet morphology (Figure S28a in the Supporting Information). In addition, the assembled electrolyzer exhibits excellent water-splitting performance, delivering a current density of 10 mA cm^{-2} at approximately 1.59 V consistently over a period of 60 h

(Figure S28b in the Supporting Information). This potential value of our assembled water-splitting device is lower othan r comparable to those in previous reports (Table S2 in the Supporting Information). In the end, the aforementioned result demonstrates the feasibility of using MoO_2-Ni in an operational water electrolysis setup.

■ **CONCLUSION**

In summary, we have constructed MoO_2-Ni heterostructured nanowires by a facile gradient pyrolysis strategy of molybdates. The in situ pyrolysis and phase separation of molybdates promote the formation of intimate interfaces, which facilitates the electronic interaction between MoO_2 and Ni. In the MoO_2-Ni heterostructured nanowires, an effective charge transfer from Ni to MoO_2 is achieved, leading to a low work function, interfacial charge polarization, and promoted HER processes. We have demonstrated that the pyrolysis temperature of the catalysts and the intimate MoO_2-Ni interfaces greatly influence the HER kinetics. The optimal MoO_2-Ni NWs/NF obtained via calcination at a moderate temperature of 550 °C exhibits a Pt-like HER activity with η_{10} = 47 mV and good durability of over 50 h in 1 M KOH. The in situ Raman results demonstrate the excellent compositional stability of the MoO_2-Ni heterostructure during the alkaline HER process. Theoretical calculations suggest that the catalytic sites are on the oxygen atoms at the MoO_2-Ni interfaces, where the concentrated charge exists. The upraised O 2p orbital in MoO_2 after Ni incorporation leads to a stronger hydrogen−oxygen interaction and consequently enhances HER activity. When MoO_2-Ni is paired with the nickel−iron sulfide oxygen-evolving catalyst in a water-splitting device, it delivers 10 mA cm^{-2} at 1.59 V for continuous operation of over 60 h. The gradient pyrolysis synthetic strategy of heterostructures and the upraised atomic orbital promoted catalytic mechanism may open an exciting direction for achieving high-efficiency Pt-alternative HER electrocatalysts.

■ **EXPERIMENTAL SECTION**

Synthesis of MoO_2-Ni and MoO_2 Catalysts. The synthesis procedure for $NiMoO_4 \cdot xH_2O$ powders and nanowire

arrays on nickel foam can be found in a previous report.[62] Next, the obtained $NiMoO_4 \cdot xH_2O$ precursors (powders and nanowire arrays) were calcined stepwise without a change in the nanowire morphology. The precursors were first calcined at 280 °C and then uninterruptedly calcined at 500−600 °C in Ar/H_2 for 2 h to obtain MoO_2-Ni heterostructured nanowires. The MoO_2 mesoporous nanowires were obtained after soaking the MoO_2-Ni catalysts in 0.5 M H_2SO_4 for at least 48 h. The mass loadings of three MoO_2-Ni NWs/NF samples are ∼2.2 mg cm^{-2}.

Synthesis of Nickel−Iron Sulfide Nanosheets Grown on Carbon Cloth (NiFe-S/CC). The synthesis procedure for the CC-supported NiFe-LDH precursor (NiFe-LDH/CC) can be found in a previous report.[63] Next, the NiFe-LDH/CC and 500 mg of fresh sulfur powder were placed at two separate positions in an alumina boat with the sulfur powder at the upstream position. The sample was heated at 350 °C for 2 h under an Ar atmosphere. Finally, nickel−iron sulfide nanosheets grown on carbon cloth (NiFe-S/CC) were obtained.

Synthesis of MoO₂-Ag Heterostructured Nanowires. A 25 mL portion of $AgNO_3$ solution (0.02 M) was slowly added to 25 mL of $NaMoO_4$ solution (0.01 M), and then 100 μL of HNO_3 (68 wt %) was added to this solution. After that, the mixture was transferred to a 50 mL Teflon-lined sealed autoclave and maintained at 150 °C for 12 h. The obtained solid product (Ag-Mo-O precursor) was washed with distilled water five times and dried under vacuum for 12 h. Next, the Ag-Mo-O precursor was calcined at 280 °C and then uninterruptedly calcined at 500 °C under Ar/H_2 for 2 h to obtain MoO_2-Ag heterostructured nanowires.

Characterization. The catalysts were characterized by XRD (using a Bruker D8 Advance X-ray diffractometer with Cu Kα radiation (λ = 1.54060 Å)), XPS and UPS (using an ESCALAB 250Xi instrument), and ICP (PerkinElmer Optima 4300DV spectrometer). Scanning electron microscopy (SEM) was carried out using a JEOL-7100F microscope at an acceleration voltage of 20 kV. TEM, HRTE,M and HAADF-STEM were collected using a JEM-2100F/Titan G2 60-300 transmission electron microscope. The in situ images were obtained by an in situ holder (DENSsolutions Climate S3 Plus) and HRTEM (Talos F200X, FEI) at an accelerating voltage of 200 kV for the electron beam. BET specific surface area characterizations were measured using a Tristar II 3020 instrument by adsorption of nitrogen at 77 K. In situ Raman spectra were recorded using a HORIBA HR EVO Raman spectroscopy system with 633 nm laser. Each spectrum was recorded (150 s duration and 50 s interval) on the MoO_2-Ni NWs/NF, and meanwhile the chronopotentiometric measurements were carried out at −1.4 mA in 1 M KOH during in situ Raman testing.

Electrochemical Measurements. Electrochemical measurements were performed with a CHI760E electrochemical analyzer in a standard three-electrode system using a graphite plate as the counter electrode and an Hg/HgO electrode (used in alkaline solution) or saturated calomel electrode (SCE, used in acidic solution) as the reference electrode. MoO_2-Ni NWs/NF was directly used as a working electrode. For the powdered catalysts, 12 mg of the catalyst was dispersed in 1 mL of a mixed solution (0.25 mL of ethanol, 0.7 mL of H_2O, and 0.05 mL of Nafion solution (5 wt %)) followed by ultrasonication for 30 min to obtain a homogeneous ink; then the working electrode for the HER was prepared by dripping 9 μL of the ink on glassy carbon (3 mm in diameter) and dried in air. In alkaline solution, the potential was referenced to a RHE on the basis of the following equation: $E(RHE) = E(Hg/HgO) + 0.098\ V + 0.0592 \times pH$. In acid, the equation is $E(RHE) = E(SCE) + 0.2415\ V + 0.0592 \times pH$. Herein, the measured pH values of 0.5 M H_2SO_4 and 1 M KOH are 0.3 and 13.8, respectively. LSV curves were all corrected by iR compensation. For the catalysts grown on nickel foam, the CV and LSV curves were normalized by the geometric area of nickel foam.

Calculation Method. All of the calculations were done by using the Vienna ab initio simulation package (VASP)[64] accompanied by VTST tools.[65] The plane wave basis set cutoff energy was 480 eV for geometry optimization and single energy calculation. A generalized gradient approximation (GGA)[66] with the Perdew−Burke−Ernzerhof (PBE) function[67] was used to describe exchange-correlation interactions. Gaussian smearing was employed with a σ value of 0.1 eV for single energy calculation. The energy convergence tolerance for the self-consistent field (SCF) was 0.01 meV. The force convergence tolerance for geometry optimization was considered as 0.05 eV/Å. All calculations were done with spin unrestricted. The surface models with or without hydrogen adsorbate were first optimized with $1 \times 1 \times 1$ γ-centered k points, and then calculated single-point energies with $2 \times 2 \times 1$ γ-centered k points to get accurate adsorption energies. On the basis of our test, a $2 \times 2 \times 1$ k point setting was dense enough and has negligible energy error in comparison to a $3 \times 3 \times 1$ k-point setting. In addition, ΔG_w is calculated as the energy difference between the transition state and the complex.

■ ASSOCIATED CONTENT

ⓢ Supporting Information

The Supporting Information is available free of charge on the ACS Publications website at DOI: 10.1021/acscatal.8b04817.

    Additional figures and tables as described in the text (PDF)

■ AUTHOR INFORMATION

Corresponding Authors
*E-mail for W.X.: weiandna1234@163.com.
*E-mail for X.W.: xjwu@ustc.edu.cn.
*E-mail for L.M.: mlq518@whut.edu.cn.

ORCID 🄳
Yanwu Zhu: 0000-0002-7505-1502
Xiaojun Wu: 0000-0003-3606-1211
Liqiang Mai: 0000-0003-4259-7725

Author Contributions
∥X.L., K.N., and C.N. contributed equally to this work.

Author Contributions
X.L. C.N., and L.M. designed the experiments, analyzed the results, and wrote the manuscript. X.L., R.G., and J.M. performed the experiments and analyzed the results. K.N., X.W., and X.L. performed the DFT computations and theoretical analyses. X.L., W.X., and J.L. carried out the in situ TEM experiments and related analyses. All authors have read and commented on the manuscript and have given approval to the final version of the manuscript.

Notes
The authors declare no competing financial interest.

Research Article

REFERENCES

(1) Turner, J. A. Sustainable Hydrogen Production. *Science* **2004**, *305*, 972−974.

(2) Chu, S.; Majumdar, A. Opportunities and Challenges for a Sustainable Energy Future. *Nature* **2012**, *488*, 294−303.

(3) Zou, X. X.; Zhang, Y. Noble Metal-Free Hydrogen Evolution Catalysts for Water Splitting. *Chem. Soc. Rev.* **2015**, *44*, 5148−5180.

(4) Ren, B. W.; Li, D. Q.; Jin, Q. Y.; Cui, H.; Wang, C. X. Integrated 3D Self-Supported Ni Decorated MoO_2 Nanowires as Highly Efficient Electrocatalysts for Ultra-Highly Stable and Large-Current-Density Hydrogen Evolution. *J. Mater. Chem. A* **2017**, *5*, 24453−24461.

(5) Cobo, S.; Heidkamp, J.; Jacques, P. A.; Fize, J.; Fourmond, V.; Guetaz, L.; Jousselme, B.; Ivanova, V.; Dau, H.; Palacin, S.; Fontecave, M.; Artero, V. A Janus Cobalt-Based Catalytic Material for Electro-Splitting of Water. *Nat. Mater.* **2012**, *11*, 802−807.

(6) Wang, J.; Xu, F.; Jin, H. Y.; Chen, Y. Q.; Wang, Y. Non-Noble Metal-Based Carbon Composites in Hydrogen Evolution Reaction: Fundamentals to Applications. *Adv. Mater.* **2017**, *29*, 1605838.

(7) Meng, J. S.; Liu, X.; Li, J. T.; Li, Q.; Zhao, C.; Xu, L. H.; Wang, X. P.; Liu, F.; Yang, W.; Xu, X. M.; Liu, Z. A.; Niu, C. J.; Mai, L. Q. General Oriented Synthesis of Precise Carbon-Confined Nanostructures by Low-Pressure Metal Vapor Superassembly and Controlled Pyrolysis. *Nano Lett.* **2017**, *17*, 7773−7781.

(8) Jin, H. Y.; Guo, C. X.; Liu, X.; Liu, J. L.; Vasileff, A.; Jiao, Y.; Zheng, Y.; Qiao, S.-Z. Emerging Two-Dimensional Nanomaterials for Electrocatalysis. *Chem. Rev.* **2018**, *118*, 6337−6408.

(9) Greeley, J.; Jaramillo, T. F.; Bonde, J.; Chorkendorff, I.; Nørskov, J. K. Computational High-Throughput Screening of Electrocatalytic Materials for Hydrogen Evolution. *Nat. Mater.* **2006**, *5*, 909−913.

(10) Kumar, G.; Nikolla, E.; Linic, S.; Medlin, J. W.; Janik, M. J. Multicomponent Catalysts: Limitations and Prospects. *ACS Catal.* **2018**, *8*, 3202−3208.

(11) Bai, Y.; Huang, H.; Wang, C. M.; Long, R.; Xiong, Y. J. Engineering the Surface Charge States of Nanostructures for Enhanced Catalytic Performance. *Mater. Chem. Front.* **2017**, *1*, 1951−1964.

(12) Song, B.; Jin, S. Two are Better than One Heterostructures Improve Hydrogen Evolution Catalysis. *Joule* **2017**, *1*, 220−221.

(13) Niu, C. J.; Liu, X.; Meng, J. S.; Xu, L.; Yan, M. Y.; Wang, X. P.; Zhang, G. B.; Liu, Z. A.; Xu, X. M.; Mai, L. Q. Three Dimensional V_2O_5/NaV_6O_{15} Hierarchical Heterostructures: Controlled Synthesis and Synergistic Effect Investigated by *In Situ* X-ray Diffraction. *Nano Energy* **2016**, *27*, 147−156.

(14) Mai, L. Q.; Yang, F.; Zhao, Y. L.; Xu, X.; Xu, L.; Luo, Y. Z. Hierarchical $MnMoO_4/CoMoO_4$ Heterostructured Nanowires with Enhanced Supercapacitor Performance. *Nat. Commun.* **2011**, *2*, 381.

(15) Tackett, B. M.; Sheng, W. C.; Chen, J. G. Opportunities and Challenges in Utilizing Metal-Modified Transition Metal Carbides as Low-Cost Electrocatalysts. *Joule* **2017**, *1*, 253−263.

(16) Zhang, J.; Wang, T.; Liu, P.; Liao, Z. Q.; Liu, S. H.; Zhuang, X. D.; Chen, M. W.; Zschech, E.; Feng, X. L. Efficient Hydrogen Production on $MoNi_4$ Electrocatalysts with Fast Water Dissociation Kinetics. *Nat. Commun.* **2017**, *8*, 15437.

(17) Lu, Q. P.; Wang, A. L.; Gong, Y.; Hao, W.; Cheng, H. F.; Chen, J. Z.; Li, B.; Yang, N. L.; Niu, W. X.; Wang, J.; Yu, Y. F.; Zhang, X.; Chen, Y.; Fan, Z. X.; Wu, X. J.; Chen, J. P.; Luo, J.; Li, S. Z.; Gu, L.; Zhang, H. Crystal Phase-Based Epitaxial Growth of Hybrid Noble Metal Nanostructures on 4H/fcc Au Nanowires. *Nat. Chem.* **2018**, *10*, 456−461.

(18) Ng, J. W. D.; Melchor, M. G.; Bajdich, M.; Chakthranont, P.; Kirk, C.; Vojvodic, A.; Jaramillo, T. F. Gold-Supported Cerium-Doped NiO_x Catalysts for Water Oxidation. *Nat. Energy* **2016**, *1*, 16053.

(19) Gong, M.; Zhou, W.; Tsai, M. C.; Zhou, J. G.; Guan, M. Y.; Lin, M. C.; Zhang, B.; Hu, Y. F.; Wang, D. Y.; Yang, J.; Pennycook, S. J.; Hwang, B. J.; Dai, H. J. Nanoscale Nickel Oxide/Nickel Heterostructures for Active Hydrogen Evolution Electrocatalysis. *Nat. Commun.* **2014**, *5*, 4695.

(20) Zhu, C. R.; Wang, A. L.; Xiao, W.; Chao, D. L.; Zhang, X.; Tiep, N. H.; Chen, S.; Kang, J. N.; Wang, X.; Ding, J.; Wang, J.; Zhang, H.; Fan, H. J. In Situ Grown Epitaxial Heterojunction Exhibits High-Performance Electrocatalytic Water Splitting. *Adv. Mater.* **2018**, *30*, 1705516.

(21) Feng, J. X.; Wu, J. Q.; Tong, Y. X.; Li, G. R. Efficient Hydrogen Evolution on Cu Nanodots-Decorated Ni_3S_2 Nanotubes by Optimizing Atomic Hydrogen Adsorption and Desorption. *J. Am. Chem. Soc.* **2018**, *140*, 610−617.

(22) Zhao, S.; Jin, R. X.; Abroshan, H.; Zeng, C. J.; Zhang, H.; House, S. D.; Gottlieb, E.; Kim, H. J.; Yang, J. C.; Jin, R. C. Gold Nanoclusters Promote Electrocatalytic Water Oxidation at the Nanocluster/$CoSe_2$ Interface. *J. Am. Chem. Soc.* **2017**, *139*, 1077−1080.

(23) Wang, P. T.; Zhang, X.; Zhang, J.; Wan, S.; Guo, S. J.; Lu, G.; Yao, J. L.; Huang, X. Q. Precise Tuning in Platinum-Nickel/Nickel Sulfide Interface Nanowires for Synergistic Hydrogen Evolution Catalysis. *Nat. Commun.* **2017**, *8*, 14580.

(24) Subbaraman, R.; Tripkovic, D.; Strmcnik, D.; Chang, K.-C.; Uchimura, M.; Paulikas, A. P.; Stamenkovic, V.; Markovic, N. M. Enhancing Hydrogen Evolution Activity in Water Splitting by Tailoring Li^+-$Ni(OH)_2$-Pt Interfaces. *Science* **2011**, *334*, 1256−1260.

(25) Guo, Y. X.; Gan, L. F.; Shang, C. S.; Wang, E.; Wang, J. A Cake-Style CoS_2@MoS_2/RGO Hybrid Catalyst for Efficient Hydrogen Evolution. *Adv. Funct. Mater.* **2017**, *27*, 1602699.

(26) Feng, J. X.; Tong, S. Y.; Tong, Y. X.; Li, G. R. Pt-Like Hydrogen Evolution Electrocatalysis on PANI/CoP Hybrid Nanowires by Weakening the Shackles of Hydrogen Ions on the Surfaces of Catalysts. *J. Am. Chem. Soc.* **2018**, *140*, 5118−5126.

(27) Bae, C.; Ho, T. A.; Kim, H.; Lee, S.; Lim, S.; Kim, M.; Yoo, H.; Montero-Moreno, J. M.; Park, J. H.; Shin, H. Bulk Layered Heterojunction as an Efficient Electrocatalyst for Hydrogen Evolution. *Sci. Adv.* **2017**, *3*, e1602215.

(28) Hu, J.; Zhang, C. X.; Jiang, L.; Lin, H.; An, Y. M.; Zhou, D.; Leung, M. K. H.; Yang, S. H. Nanohybridization of MoS_2 with Layered Double Hydroxides Efficiently Synergizes the Hydrogen Evolution in Alkaline Media. *Joule* **2017**, *1*, 383−393.

(29) Jin, H. Y.; Wang, J.; Su, D. F.; Wei, Z. Z.; Pang, Z. F.; Wang, Y. In Situ Cobalt-Cobalt Oxide/N-Doped Carbon Hybrids as Superior Bifunctional Electrocatalysts for Hydrogen and Oxygen Evolution. *J. Am. Chem. Soc.* **2015**, *137*, 2688−2694.

(30) Wen, W.; Calderon, J. E.; Brito, J. L.; Marinkovic, N.; Hanson, J. C.; Rodriguez, J. A. In Situ Time-Resolved Characterization of Ni-MoO_2 Catalysts for the Water-Gas Shift Reaction. *J. Phys. Chem. C* **2008**, *112*, 2121−2128.

(31) Greiner, M. T.; Chai, L.; Helander, M. G.; Tang, W. M.; Lu, Z. H. Metal/Metal-Oxide Interfaces: How Metal Contacts Affect the Work Function and Band Structure of MoO_3. *Adv. Funct. Mater.* **2013**, *23*, 215−226.

(32) Yan, X. D.; Tian, L. H.; He, M.; Chen, X. B. Three-Dimensional Crystalline/Amorphous Co/Co_3O_4 Core/Shell Nanosheets as Efficient Electrocatalysts for the Hydrogen Evolution Reaction. *Nano Lett.* **2015**, *15*, 6015−6021.

(33) Weng, Z.; Liu, W.; Yin, L.-C.; Fang, R. P.; Li, M.; Altman, E. I.; Fan, Q.; Li, F.; Cheng, H. M.; Wang, H. L. Metal/Oxide Interface Nanostructures Generated by Surface Segregation For Electrocatalysis. *Nano Lett.* **2015**, *15*, 7704−7710.

(34) Liu, X. E.; Liu, W.; Ko, M.; Park, M.; Kim, M. G.; Oh, P.; Chae, S.; Park, S.; Casimir, A.; Wu, G.; Cho, J. Metal (Ni, Co)-Metal Oxides/Graphene Nanocomposites as Multifunctional Electrocatalysts. *Adv. Funct. Mater.* **2015**, *25*, 5799−5808.

(35) Wu, R.; Zhang, J. F.; Shi, Y. M.; Liu, D. L.; Zhang, B. Metallic WO₂-Carbon Mesoporous Nanowires as Highly Efficient Electrocatalysts for Hydrogen Evolution Reaction. *J. Am. Chem. Soc.* **2015**, *137*, 6983−6986.

(36) Ito, Y.; Ohto, T.; Hojo, D.; Wakisaka, M.; Nagata, Y.; Chen, L. H.; Hu, K. L.; Izumi, M.; Fujita, J.; Adschiri, T. Cooperation Between Holey Graphene and NiMo Alloy for Hydrogen Evolution in an Acidic Electrolyte. *ACS Catal.* **2018**, *8*, 3579−3586.

(37) Jiang, P.; Yang, Y.; Shi, R. H.; Xia, G. L.; Chen, J. T.; Su, J. W.; Chen, Q. W. Pt-Like Electrocatalytic Behavior of Ru-MoO₂ Nanocomposites for the Hydrogen Evolution Reaction. *J. Mater. Chem. A* **2017**, *5*, 5475−5485.

(38) Zhang, Z.; Ma, X. X.; Tang, J. L. Porous NiMoO₄₋ₓ/MoO₂ Hybrids as Highly Effective Electrocatalysts for the Water Splitting Reaction. *J. Mater. Chem. A* **2018**, *6*, 12361−12369.

(39) Chen, Y. Y.; Zhang, Y.; Zhang, X.; Tang, T.; Luo, H.; Niu, S.; Dai, Z. H.; Wan, L. J.; Hu, J. S. Self-Templated Fabrication of MoNi₄/MoO₃₋ₓ Nanorod Arrays with Dual Active Components for Highly Efficient Hydrogen Evolution. *Adv. Mater.* **2017**, *29*, 1703311.

(40) An, Q. Y.; Lv, F.; Liu, Q. Q.; Han, C. H.; Zhao, K. N.; Sheng, J. Z.; Wei, Q. L.; Yan, M. Y.; Mai, L. Q. Amorphous Vanadium Oxide Matrixes Supporting Hierarchical Porous Fe₃O₄/Graphene Nanowires as a High-Rate Lithium Storage Anode. *Nano Lett.* **2014**, *14*, 6250−6256.

(41) Tang, C. J.; Liu, Y. N.; Xu, C.; Zhu, J. X.; Wei, X. J.; Zhou, L.; He, L.; Yang, W.; Mai, L. Q. Ultrafine Nickel-Nanoparticle-Enabled SiO₂ Hierarchical Hollow Spheres for High-Performance Lithium Storage. *Adv. Funct. Mater.* **2018**, *28*, 1704561.

(42) Hu, E. L.; Feng, Y. F.; Nai, J. W.; Zhao, D.; Hu, Y.; Lou, X. W. Construction of Hierarchical Ni-Co-P Hollow Nanobricks with Oriented Nanosheets for Efficient Overall Water Splitting. *Energy Environ. Sci.* **2018**, *11*, 872−880.

(43) Fang, Z. W.; Peng, L. L.; Qian, Y. M.; Zhang, X.; Xie, Y. J.; Cha, J. J.; Yu, G. H. Dual Tuning of Ni-Co-A (A = P, Se, O) Nanosheets by Anion Substitution and Holey Engineering For Efficient Hydrogen Evolution. *J. Am. Chem. Soc.* **2018**, *140*, 5241−5247.

(44) Fan, L. L.; Liu, P. F.; Yan, X. C.; Gu, L.; Yang, Z. Z.; Yang, H. G.; Qiu, S. L.; Yao, X. D. Atomically Isolated Nickel Species Anchored on Graphitized Carbon for Efficient Hydrogen Evolution Electrocatalysis. *Nat. Commun.* **2016**, *7*, 10667.

(45) Kuang, Y.; Feng, G.; Li, P. S.; Bi, Y. M.; Li, Y. P.; Sun, X. M. Single-Crystalline Ultrathin Nickel Nanosheets Array from In Situ Topotactic Reduction for Active and Stable Electrocatalysis. *Angew. Chem., Int. Ed.* **2016**, *55*, 693−697.

(46) Cheng, Z. H.; Fu, Q.; Han, Q.; Xiao, Y. K.; Liang, Y.; Zhao, Y.; Qu, L. T. A Type of 1 nm Molybdenum Carbide Confined within Carbon Nanomesh as Highly Efficient Bifunctional Electrocatalyst. *Adv. Funct. Mater.* **2018**, *28*, 1705967.

(47) Mahmood, J.; Li, F.; Jung, S. M.; Okyay, M. S.; Ahmad, I.; Kim, S. J.; Park, N.; Jeong, H. Y.; Baek, J. B. An Efficient and pH-Universal Ruthenium-Based Catalyst for the Hydrogen Evolution Reaction. *Nat. Nanotechnol.* **2017**, *12*, 441−446.

(48) Feng, L. L.; Yu, G. T.; Wu, Y. Y.; Li, G. D.; Li, H.; Sun, Y. H.; Asefa, T.; Chen, W.; Zou, X. X. High-Index Faceted Ni₃S₂ Nanosheet Arrays as Highly Active and Ultrastable Electrocatalysts for Water Splitting. *J. Am. Chem. Soc.* **2015**, *137*, 14023−14026.

(49) Zhang, L. H.; Han, L. L.; Liu, H. X.; Liu, X. J.; Luo, J. Potential-Cycling Synthesis of Single Platinum Atoms for Efficient Hydrogen Evolution in Neutral Media. *Angew. Chem., Int. Ed.* **2017**, *56*, 13694−13698.

(50) Dieterle, M.; Mestl, G. Raman Spectroscopy of Molybdenum Oxides. Part II. Resonance Raman Spectroscopic Characterization of the Molybdenum Oxides Mo₄O₁₁ and MoO₂. *Phys. Chem. Chem. Phys.* **2002**, *4*, 822−826.

(51) Jin, Y. S.; Wang, H. T.; Li, J. J.; Yue, X.; Han, Y. J.; Shen, P. K.; Cui, Y. Porous MoO₂ Nanosheets as Non-Noble Bifunctional Electrocatalysts for Overall Water Splitting. *Adv. Mater.* **2016**, *28*, 3785−3790.

(52) Jin, H. Y.; Liu, X.; Jiao, Y.; Vasileff, A.; Zheng, Y.; Qiao, S.-Z. Constructing Tunable Dual Active Sites on Two-Dimensional C₃N₄@MoN Hybrid for Electrocatalytic Hydrogen Evolution. *Nano Energy* **2018**, *53*, 690−697.

(53) Ling, T.; Yan, D.-Y.; Wang, H.; Jiao, Y.; Hu, Z. P.; Zheng, Y.; Zheng, L. R.; Mao, J.; Liu, H.; Du, X.-W.; Jaroniec, M.; Qiao, S.-Z. Activating Cobalt(II) Oxide Nanorods for Efficient Electrocatalysis by Strain Engineering. *Nat. Commun.* **2017**, *8*, 1509.

(54) Yu, H. D.; Xue, Y. R.; Hui, L.; Zhang, C.; Li, Y. J.; Zuo, Z. C.; Zhao, Y. J.; Li, Z. B.; Li, Y. L. Efficient Hydrogen Production on a 3D Flexible Heterojunction Material. *Adv. Mater.* **2018**, *30*, 1707082.

(55) Wang, S.; Zheng, M. H.; Li, M.; Wu, X. J.; Xia, C. R. Synergistic Effects towards H₂ Oxidation on the Cu-CeO₂ Electrode: A Combination Study with DFT Calculations and Experiments. *J. Mater. Chem. A* **2016**, *4*, 5745−5754.

(56) Zheng, Y.; Jiao, Y.; Vasileff, A.; Qiao, S.-Z. The Hydrogen Evolution Reaction in Alkaline Solution: From Theory, Single Crystal Models, to Practical Electrocatalysts. *Angew. Chem., Int. Ed.* **2018**, *57*, 7568−7579.

(57) Chen, G. B.; Wang, T.; Zhang, J.; Liu, P.; Sun, H. J.; Zhuang, X. D.; Chen, M. W.; Feng, X. L. Accelerated Hydrogen Evolution Kinetics on NiFe-Layered Double Hydroxide Electrocatalysts by Tailoring Water Dissociation Active Sites. *Adv. Mater.* **2018**, *30*, 1706279.

(58) Miao, R.; Dutta, B.; Sahoo, S.; He, J. K.; Zhong, W.; Cetegen, S. A.; Jiang, T.; Alpay, S. P.; Suib, S. L. Mesoporous Iron Sulfide for Highly Efficient Electrocatalytic Hydrogen Evolution. *J. Am. Chem. Soc.* **2017**, *139*, 13604−13607.

(59) Zhu, Z. J.; Yin, H. J.; He, C. T.; Al-Mamun, M.; Liu, P. R.; Jiang, L. X.; Zhao, Y.; Wang, Y.; Yang, H. G.; Tang, Z. Y.; Wang, D.; Chen, X. M.; Zhao, H. J. Ultrathin Transition Metal Dichalcogenide/3d Metal Hydroxide Hybridized Nanosheets to Enhance Hydrogen Evolution Activity. *Adv. Mater.* **2018**, *30*, 1801171.

(60) Voiry, D.; Yamaguchi, H.; Li, J. W.; Silva, R.; Alves, D. C. B.; Fujita, T.; Chen, M. W.; Asefa, T.; Shenoy, V. B.; Eda, G.; Chhowalla, M. Enhanced Catalytic Activity in Strained Chemically Exfoliated WS₂ Nanosheets for Hydrogen Evolution. *Nat. Mater.* **2013**, *12*, 850−855.

(61) Liu, X.; Ni, K.; Wen, B.; Niu, C. J.; Meng, J. S.; Guo, R. T.; Li, Q.; Li, J. T.; Zhu, Y. W.; Wu, X. J.; Zhao, D. Y.; Mai, L. Q. Polyoxomolybdate-Derived Carbon-Encapsulated Multicomponent Electrocatalysts for Synergistically Boosting Hydrogen Evolution. *J. Mater. Chem. A* **2018**, *6*, 17874−17881.

(62) Peng, S. J.; Li, L. L.; Wu, H. B.; Madhavi, S.; Lou, X. W. Controlled Growth of NiMoO₄ Nanosheet and Nanorod Arrays on Various Conductive Substrates as Advanced Electrodes for Asymmetric Supercapacitors. *Adv. Energy Mater.* **2015**, *5*, 1401172.

(63) Wang, Z. Y.; Li, J. T.; Tian, X. C.; Wang, X. P.; Yu, Y.; Owusu, K. A.; He, L.; Mai, L. Q. Porous Nickel-Iron Selenide Nanosheets as Highly Efficient Electrocatalysts for Oxygen Evolution Reaction. *ACS Appl. Mater. Interfaces* **2016**, *8*, 19386−19392.

(64) Hafner, J. Ab-Initio Simulations of Materials Using VASP: Density-Functional Theory and Beyond. *J. Comput. Chem.* **2008**, *29*, 2044−2078.

(65) Henkelman, G.; Uberuaga, B. P.; Jónsson, H. A Climbing Image Nudged Elastic Band Method for Finding Saddle Points and Minimum Energy Paths. *J. Chem. Phys.* **2000**, *113*, 9901−9904.

(66) Perdew, J. P.; Burke, K.; Ernzerhof, M. Generalized Gradient Approximation Made Simple. *Phys. Rev. Lett.* **1996**, *77*, 3865−3868.

(67) Ernzerhof, M.; Scuseria, G. E. Assessment of the Perdew-Burke-Ernzerh of Exchange-Correlation Functional. *J. Chem. Phys.* **1999**, *110*, 5029−5036.